

**Impact of Varying Lidar Measurement and Data Processing Techniques in
evaluating Cirrus Cloud and Aerosol Direct Radiative Effects.**

S. Lolli^{1,2, 1}, F. Madonna¹, M. Rosoldi¹, J. R. Campbell³, E. J. Welton⁴ J. R. Lewis², Y.
Gu⁵, G. Pappalardo¹

¹ CNR-IMAA, Istituto di Metodologie Ambientali Tito Scalo (PZ), Italy

² NASA GSFC-JCET, Code 612, 20771 Greenbelt, MD, USA

³Naval Research Laboratory, Monterey, CA, USA

⁴NASA GSFC, Code 612, 20771 Greenbelt, MD, USA

⁵UCLA, University of California Los Angeles, Los Angeles, USA

ABSTRACT

During the last two decades, ground-based lidar networks have drastically increased in scope and relevance, thanks primarily to the advent of lidar observations from space and need for validation. Lidar observations of aerosol and cloud geometrical and optical atmospheric properties are used to evaluate their direct radiative effects on climate. However, the retrievals are strongly dependent on the employed lidar instrument measurement technique and subsequent data processing methodologies. In this paper, we evaluate discrepancies between the use of Raman and elastic lidar measurement techniques and corresponding data processing methods for two aerosol layers in the free troposphere and for thin versus opaque cirrus clouds. The different lidar techniques are responsible of larger discrepancies in direct radiative effects for biomass burning (0.05 W/m² at surface and 0.007 W/m² at top of the atmosphere) and dust aerosol layers (0.7 W/m² at surface and 0.85 W/m² at top of the atmosphere).

¹ Corresponding author: simone.lolli@imaa.cnr.it

On the contrary, data processing is responsible for larger discrepancies on both thin (0.55 W/m^2 at surface and 2.7 W/m^2 at top of the atmosphere) and opaque (7.7 W/m^2 at surface and 11.8 W/m^2 at top of the atmosphere) cirrus clouds. Direct radiative effect discrepancies can be attributed to the larger variability of the lidar ratio for aerosols (20-150 sr) with respect to clouds (25-35 sr). For this reason, the influence of lidar technique applied plays a more fundamental role in aerosol monitoring because the lidar ratio must be retrieved with relatively high accuracy. On the contrary, for cirrus clouds, as the lidar ratio is much less variable, the data processing is of fundamental importance because different processing is modifying the extinction profile that translates into ice crystal creation/suppression ice crystals with consequent different direct radiative effect values.

1. Introduction

According to the International Panel for Climate Change (IPCC, 2014), the major sources of uncertainty relating to current climate studies include direct and indirect radiative effects caused by anthropogenic and natural aerosols. Further, current estimates of the global aerosol direct radiative effect remain subject to large relative uncertainties affecting even the actual sign (indicating either net cooling or heating of the earth-atmosphere system), which may change from positive to negative diurnally (e.g., Campbell et al., 2016, Lolli et al., 2017a). This depends on the so-called albedo effect (or the capability of aerosols of reflecting the incoming solar light) and whether or not it is outweighing the greenhouse effect (or the capability of trapping/absorbing outgoing longwave radiation; Campbell et al., 2016)

Studies on cloud and aerosol optical and geometrical properties largely increased in the last two decades through the increasing abundance of passive ground-based measurements (i.e., AErosol RObotic NETwork Network; AERONET Holben et al., 1998, Dubovik et al., 2000, Smirnov et al., 2005, Eck et al., 2014; the Atmospheric Radiation Measurement program, Campbell et al., 2002, Ferrare et al., 2006, Perez-Ramirez et al., 2014, McComiskey et al., 2016; Aerosols, Clouds and Trace gases Research Infrastructure, Asmi et al., 2013, Pappalardo et al., 2014) or using satellite sensors (i. e. MODerate resolution Infrared Spectroradiometer; MODIS, Tanré et al., 1997, King et al., 2003, Remer et al., 2005; i. e. Multi-angle Imaging Spectro-Radiometer; MISR, Diner et al., 1998, Di Girolamo et al., 2004, Kahn et al., 2009; i.e. Polarization and Anisotropy of Reflectances for Atmospheric science coupled with Observations from a Lidar; PARASOL, Tanré et al., 2011; NASA Aerosol-Cloud Ecosystem, Whiteman et al., 2017). Nevertheless, these measurements provide only an estimate of the columnar aerosol (or cloud) optical properties.

On the other hand, the Cloud-Aerosol Lidar with Orthogonal Polarization (CALIOP; Winker et al., 2007), on board of the Cloud-Aerosol Lidar and Infrared Pathfinder Satellite Observations (CALIPSO) satellite launched by the National Aeronautics and Space Administration (NASA) in 2006, is capable of estimating range-resolved aerosol and cloud physical properties. However, the sun-synchronous orbit limits spatial and temporal coverage (orbital revisit time period of 16 days) that make the datasets difficult to apply and interpret for specific forms of process study. The vertical structure of cloud and aerosol properties can also be retrieved through combined lidar and radar ground-based measurements as proposed in the frame of the CloudNet European Project

(Illingworth et al., 2015). Still, the radar technique proves capable of characterizing only the relatively extreme fraction of the aerosol size distribution (Madonna et al., 2010, Madonna et al., 2013).

Based on the progress in optical technologies in the late 1990's and the beginning of 2000's, federated ground networks of lidars were established [NASA Micro Pulse Lidar NETwork(MPLNET), Campbell et al., 2002, Welton et al., 2002, Lolli et al., 2013; European Aerosol Research Lidar NETwork, (EARLINET) Pappalardo et al., 2014, Asian Dust NETwork (ADNET), Sugimoto et al., 2010, Latin American Lidar NETwork (LALINET), Antuña-Marrero et al., 2015, Lolli et al., 2015], the bulk of which are based on single or dual-channel elastic and Raman lidar instruments. The Eulerian viewpoint of ground-based lidars is providing important contextual measurements relative to satellite profiling, like from CALIOP (Winker et al., 2007).

The emerging prominence of ground-based lidar, however, strengthens the necessity for further studies of optical and geometrical aerosols and clouds properties resolved from multi-spectral lidar techniques, as claimed by several papers (Pappalardo et al., 2004, Mona et al., 2006, Wang et al., 2012, Pani et al., 2016, Lolli et al., 2013, Campbell et al., 2016, Lolli et al., 2017). Multi-spectral and Raman lidars can retrieve aerosol and cloud properties with much better accuracy without many fundamental assumptions, (e.g., Grund and Eloranta, 1991; Ansmann et al., 1992; Goldsmith et al. 1998, Mona et al., 2012, Pappalardo et al., 2014), though with greater operational expenses. In contrast, elastic-scattering lidar instruments require such assumptions and careful consideration of measurement strategies to constrain the lidar equation (Eq. 1), defined as

$$P_r(r) = K \frac{\beta(r)}{r^2} \exp^{-2 \int_0^r \alpha(r') dr'}$$

(1)

where $P_r(r)$ is the received power at a range r , K is the so-called lidar constant (instrument dependent, function of detector quantum and optical efficiencies, telescope diameter, instrument overlap function, etc.), followed by the two unknown variables, $\beta(r)$ the total backscattering coefficient and $\alpha(r)$ the total extinction coefficient.

A classical method to solving Eq. (1) for single-channel elastic-backscatter lidars (Fernald, 1984) is based on the assumption of the columnar-averaged value of the ratio between the two unknown coefficients, typically indicated by S and called “lidar ratio”. The method, due to the large variability of S (i.e., 20-150 sr for aerosols; Ackermann, 1998) translates into large uncertainties associated with the retrieval of α and β (Lolli et al., 2013).

Through a greater spectral complexity, it is possible to retrieve α and β with multi-spectra lidars without relying too heavily on fundamental assumptions. For instance, the combined detection of the elastic-backscattered radiation and inelastic backscattering from the Raman roto-vibrational spectrum of nitrogen (or oxygen), using the Raman lidar technique, permits solving Eq. (1) by substitution of a through the analytical solution of Eq. [2] as

$$a_{I_L}^{par}(r) = \frac{d/dr \left\{ \ln \left[n_R(r) / P_r(r) r^2 \right] \right\} - a_{I_L}^{mol}(r) - a_{I_R}^{mol}(r)}{1 + \left(I_L / I_R \right)^{\hat{a}}}, \quad (2)$$

where I_L is the elastic wavelength while I_R is the wavelength of the Raman scattering, $a_{I_L}^{par}(r)$ represents the particle (aerosols or clouds) extinction coefficient at elastic

112 wavelength at range r while $\mathcal{A}_{\lambda_L}^{mol}(r)$ and $\mathcal{A}_{\lambda_R}^{mol}(r)$ are the molecular extinction coefficients
 113 at wavelengths λ_L and λ_R respectively, $P_r(r)r^2$ is the detected range corrected Raman
 114 signal from range r , while $n_R(r)$ represents the number density of range-resolved
 115 scatters. The wavelength dependence of the particle extinction coefficient is described by
 116 the Ångström coefficient, \hat{a} , defined from the relation

$$117 \quad \frac{\mathcal{A}_{\lambda_L}^{par}(r)}{\mathcal{A}_{\lambda_R}^{par}(r)} = \left(\frac{\lambda_R}{\lambda_L} \right)^{\hat{a}} \quad (3)$$

118 Eq. (2) allows for independently retrieving vertically-resolved optical coefficients with
 119 only very limited *a-priori* assumptions (the Ångström coefficient should be estimated or
 120 assumed, but this estimate or assumption, involving a ratio, typically amounts to less than
 121 5% of total error; Ansmann and Müller, 2005). The particle backscattering coefficient,
 122 $\beta_{\lambda_L}^{par}(r) / \beta_{\lambda_0}^{par}(r)$, can be derived directly from the ratio of the Raman signal at λ_R and
 123 the elastic signal at λ_L .

124 However, the Raman technique exhibits instabilities in retrieving the particle
 125 extinction coefficient (Ansmann et al., 1992, Wandinger et al, 1995), and in order to
 126 reduce the random uncertainty affecting the retrieval, a smoothing of the profile is
 127 required. In turn, smoothing decreases the effective vertical resolution (Pappalardo et al.,
 128 2004, Iarlori et al., 2015) of the aerosol extinction coefficient profile.

129 In summary, employing different lidar techniques and/or processing algorithms lead
 130 to differences of the retrieved vertically-resolved aerosol optical properties, affecting the
 131 apparent significance, position and the geometry of observed aerosol and cloud layers.

The impact of these differences on various end-user applications has never been extensively evaluated. Since lidar-derived optical properties obtained from different instrument techniques are being more and more frequently used to assess the direct radiative effects of clouds and aerosols (e.g., Campbell et al., 2016, Lolli et al., 2017a), corresponding uncertainties in determining direct radiative effects, which may help reconcile inconsistencies in studies carried out at the global scale based on different lidar techniques, are compulsory, especially now that several new space missions with lidar on board have been launched (Cloud-Aerosol Transport System; CATS, McGill et al., 2015) or are scheduled very soon (European Space Agency Earth Care mission; Illingworth et al., 2015).

The objective of this paper is to evaluate the relative differences between the aerosol/cloud direct radiative effects both at surface (SFC) and at the top-of-the-atmosphere (TOA) retrieved using the aerosol/cloud optical properties estimated using a more sophisticated versus simpler lidar technique (i.e., Raman vs. elastic lidar). To reach this goal, we use the Fu-Liou-Gu (FLG; Fu and Liou, 1992, Fu and Liou, 1993, Gu et al., 2003, Gu et al., 2011, Lolli et al., 2017b) radiative transfer model to calculate the difference in net direct radiative effect for aerosols and clouds at TOA and SFC for profiles derived from both elastic and combined Raman/elastic lidar techniques.

2. Method

2.1 Fu-Liou-Gu radiative Transfer Model

To calculate aerosol and cloud direct radiative effects, we use the one-dimensional FLG radiative transfer model, developed in the early 1990's. The original code has

recently been adapted to retrieve cloud and aerosol direct radiative effects using the aerosol and cloud vertical profile of lidar extinction as input. There exist several parameterizations that provide the vertical profile of cloud microphysics using lidar-retrieved cloud extinction profile, each one with pros and cons, as showed in Comstock et al., (2007). For the purpose of this study and also considering authors past experience (Campbell et al., 2016, Lolli et al., 2017a), we parameterize cirrus clouds through the Heymsfield et al., (2014) empirical relationship conceived expressly for lidar measurements. Here, the cirrus cloud ice crystal average diameter is directly proportional to the absolute atmospheric temperature (obtained through a radiosonde, regularly launched at measurement site, or numerical reanalysis dataset). Cirrus cloud optical depth and crystal size profiles are used to calculate the single scattering albedo (SSA), phase function and asymmetry factor (AF) at each level.

Similarly, FLG calculates the direct radiative effect of aerosols as a function of the partial contribution of each aerosol species to the total optical depth at each altitude level. FLG uses a lookup table (LUT) with single scattering properties for eighteen different types of aerosols coming from the OPAC (Optical Properties of Aerosol and Clouds) database (d'Almeida et al., 1991; Tegen and Lacis, 1996; Hess et al., 1998). Among all the aerosol species, for the first of the cases discussed in Section 2.2 we assume that the dust layer is constituted by pure dust advected from Saharan region (aerosol type 17 in FLG), while in the second case we assume pure biomass burning aerosol (aerosol type 11 in FLG). Nevertheless, if the measured aerosol atmospheric profiles do not match exactly the two-selected aerosol types this does not affect the results interpretation because we are interested in evaluating the relative discrepancies among the different lidar

techniques/data processing. Therefore, what is most relevant in the approach is the application of the same parameterization to each of the different techniques/data processing.

The aerosol/cloud direct radiative effect is calculated subtracting from the FLG total sky run (where aerosols or clouds are present) the FLG run with a pristine atmosphere (control), as reported in Eq. 4:

$$DRE = FLG^{TotalSky} - FLG^{Pristine} \quad (4)$$

2.2 Analysis of direct radiative effect

For the analysis in this study, we analyzed lidar data collected with the Multi-wavelength System for Aerosols (MUSA) Lidar (Madonna et al., 2011), deployed at Consiglio Nazionale delle Ricerche (CNR), Istituto di Metodologie per l'Analisi Ambientale (IMAA) Atmospheric Observatory (CIAO) in Potenza, Italy (40.60N, 15.72E, 760m a.s.l.). MUSA is a mobile multi-wavelength lidar system based on a Nd:YAG laser source equipped with second and third harmonic generators and on a Cassegrain telescope with a primary mirror of 300mm diameter. MUSA full angle field-of-view (FOV) is large enough (about 1.5 mrad) to add important multiple scattering (MS) contributions to the retrieved extinction profile. However, for the purpose of this study we are interested in evaluating the relative discrepancies between different lidar techniques/data processing, and therefore, at this stage, do not correct for any MS contributions since we assume that this effect impacts equally both techniques and subsequent data processing.

The three laser beams at 1064, 532 and 355nm are simultaneously and coaxially transmitted into the atmosphere in biaxial configuration. The receiving system has 3 channels for the detection of the radiation elastically backscattered from the atmosphere and 2 channels for the detection of the Raman radiation backscattered by the atmospheric N₂ molecules at 607 and 387 nm. The elastic channel at 532 nm is split into parallel and perpendicular polarization components by means of a polarizer beamsplitter cube. The backscattered radiation at all the wavelengths is acquired both in analog and photon counting mode. The typical vertical resolution of the raw profiles is 3.75 m with a temporal resolution of 1 min. The system is compact and transportable. It has operated since 2009, and it is one of the reference systems used for the intercomparison of lidar systems within EARLINET (Pappalardo et al., 2014; Wandinger et al., 2016) Quality Assurance program. In this paper, the data analysis has been carried out considering four observation scenarios at night, as the Raman channel signal shows a much higher signal-to-noise ratio during nighttime:

- 1) **Dense Dust Aerosol and Biomass Burning Events**. The aerosol extinction profiles are retrieved using the UV (355nm) channel. For each case, the extinction profile is retrieved both with the Raman technique (Ansmann et al., 1990, Whiteman et al., 1992, Veselovskii et al., 2015) and estimated using the sole elastic channel, applying an iterative algorithm (Di Girolamo et al., 1999) with an assigned lidar ratio ($S=45$ sr for dust case, Mona et al., 2006 and $S=63$ sr for biomass burning, retrieved averaging the lidar ratio from MUSA Raman channel). Both the Raman and elastic lidar signals have been smoothed by performing a binning of 16 range gates, resulting in a vertical resolution of 60 m. For the

Raman channel retrieval, the extinction profile has been calculated using the sliding linear fit technique, with a bin number resulting in an effective vertical resolution of 360 m (Pappalardo et al., 2004). For the elastic channel retrieval, the estimated extinction profile has been first calculated with the signal full vertical resolution of 60 m and then smoothed to the same effective vertical resolution as the Raman extinction profile (360m), using a 2nd order Savitzky-Golay smoothing filter (Press et al., 1992; Iarlori et al., 2015).

2) **Thin and Opaque Cirrus Clouds**. Like aerosols, cirrus cloud extinction profiles are retrieved using the UV (355nm) channel with the Raman technique. The elastic channel retrieval for thin cirrus cloud is obtained applying the same iterative algorithm followed for dust and biomass burning. Although, for the opaque cirrus cloud, due to convergence problems of the iterative method for higher cloud optical depths, we used the MPLNET Level 1.5 cloud product algorithm (Lewis et al., 2016) based on a Klett inversion (Klett, 1985). For both cases (iterative and MPLNET), we assumed a fix lidar ratio value of 25sr (Campbell et al., 2016, Lolli et al., 2017a). The Raman extinction profile has been calculated with an effective vertical resolution of 420 m (thin cirrus cloud) and 780 m (opaque cirrus cloud), respectively. The iterative (thin cirrus) and MPLNET Level 1.5 cloud algorithm (opaque cirrus; Lewis et al., 2016) extinction profiles are calculated with the original signal vertical resolution of 60 m and smoothed at a resolution of 420 m (thin cirrus) and 780 m (opaque cirrus), respectively, using the Savitzky-Golay filter to match Raman channel spatial resolution.

3) The thermodynamic profile of the atmosphere, needed to calculate the direct radiative effect, is estimated using a standard thermodynamic profile (USS976) mid-latitude model. Emissivity and albedo values are taken from the MODIS Bidirectional Reflectance Distribution Function (BRDF)/Albedo algorithm product (Strahler et al., 1999), with a spatial resolution of 0.1 degrees averaged over a 16-day temporal window (Campbell et al., 2016). As each measured cloud and aerosol extinction profile comes with a relative uncertainty per range bin, the sensitivity of FLG to the input parameters is evaluated applying a Monte Carlo technique. Each extinction profile is replicated 30 times (i.e. a number statistically meaningful), running the MonteCarlo code on the original profile random uncertainty. Likewise, for each replicated extinction profile, the Monte Carlo technique gives a value of surface albedo and profile temperature, based on their respective uncertainties. The direct radiative effect parameters derived for each profile are then represented with a boxplot. It is possible then to quantify the effect of the smoothing calculating the uncertainty from the mean and the standard deviation of the values of net forcing.

3. Results

3.1 Dust and Biomass Burning Event

The analyzed dust event is retrieved from measurements taken on 3 July 2014 at CIAO. Figure 1 shows both the range-corrected composite signal at 1064nm (Fig. 1a, left panel), and the lidar aerosol extinction profiles at 355nm (Fig. 1b, left panel) obtained using the Raman technique with an effective resolution of 360m and estimated using the

elastic lidar technique at two different resolutions (60m and 360m) using a fixed S value obtained analyzing climatological data ($S=45\text{sr}$; Mona et al., 2006). It can be immediately recognized that the Raman extinction profile is noisier with respect to those obtained with the iterative method. All the profiles, calculated with an integration time of 121 minutes, in the time window from 19:34UT to 21:40UT, show no significant aerosol loading above 5.5 km.

Figure 3a shows the difference between the estimation of the direct radiative effect using the two considered lidar techniques and data processing at TOA (Fig 3a, left panel) and at SFC (Fig. 3a right panel). The most important contribution to this difference in FLG calculations for this case is related to the adopted lidar technique (red arrows in Fig. 3a, left and right panels) and not to the effective vertical resolution determined by the smoothing (blue arrows in Fig. 3a, left and right panels). This characteristic is invariant switching from TOA (Fig. 3a right panel) to SFC (Fig. 3a left panel) and it is mainly the result of the assumption of a fixed lidar ratio to estimate the aerosol extinction profile using the elastic technique.

For the dust case, the net direct radiative effect determined with the two different lidar techniques differs by 0.7 W/m^2 (5%) at SFC and 0.85 W/m^2 (6%) at TOA. In absolute value, those net total forcing values are larger than the uncertainty on average estimated direct effect by IPCC (mean -0.5 W/m^2 , range -0.9 to -0.1). The contribution due to smoothing is negligible in comparison.

The analyzed biomass burning case study is retrieved from measurements taken on 19 June 2013 at CIAO integrating the signal temporally from 19:27UT to 20:48 UT. The extinction profiles used as input into the FLG radiative transfer model was retrieved in

the same way as for the dust case, but being unavailable a climatological lidar ratio value at 355nm, we used $S=63$ sr, obtained averaging the retrieved Raman channel lidar ratio in the biomass burning layer. In Figure 1b (right panel) are the extinction profiles obtained from both the Raman and iterative methods (full resolution and smoothed over 360m window). Figure 3b shows the difference in biomass burning direct radiative effects with respect to the different lidar techniques and data processing. Similar to the dust case event, the bigger differences are found to be related to the different lidar techniques both at SFC (0.05 W/m^2 or 5%; red arrows, Fig. 3b right panel) and at TOA (0.007 W/m^2 or 5%; Fig. 3b left panel).

The analysis shows how the mixing of different lidar techniques in a specific study or in the routine operations of an aerosol network at regional or global scale must take into account of the uncertainties related to the assumptions that are behind the retrieval of the optical properties. This is important not only to provide a complete assessment of the total uncertainty budget for each lidar product but also to enable a physically consistent use of the lidar data in the estimation of the direct radiative effect and, likely, for many other user-oriented applications based on lidar data.

3.2 *Cirrus cloud*

Similar to Fig.1, Fig. 2a and 2b shows the composite range-corrected signal and three extinction profiles retrieved from lidar measurements of cirrus cloud obtained with Raman channel with a vertical resolution of 420m (thin cirrus, Fig 2a,b left panel) and 780m (opaque cirrus, Fig 2a,b right panel) and with the elastic channel at two vertical resolutions (60m and 420m iterative method for thin cirrus cloud; 60m and 780m

MPLNET Level 1.5 cloud product algorithm for opaque cirrus cloud) using a lidar ratio of 25sr. The obtained cloud extinction profiles with the different lidar techniques and data processing techniques are averaged over 42 minutes, in the time window from 01:29UT to 02:13UT on 17 February 2014 (thin cirrus) and from 19:40UT to 20:44UT in 09 May 2016 (opaque cirrus), respectively.

Figure 4a depicts the results obtained for cirrus cloud measurements taken on 17 February 2014. Here we have a completely different situation with respect to the aerosol cases. That is, the discrepancies between the Raman and elastic lidar techniques (red arrows in Fig. 4a, left and right panels) are much smaller than the discrepancies due to the effective vertical resolution of the aerosol extinction coefficient profile both at TOA and SFC (blue arrows in Fig. 4a, left and right panels). This is related to the typically much stronger extinction for clouds than for aerosols. In the considered cirrus cloud case, the direct radiative effect determined with the two different lidar techniques differs of about 0.5 W/m² (9%) at TOA and 0.11 W/m² (10%) at SFC, while the effect of smoothing on a window of 420 m provides an additional difference of 2.7 W/m² (47%) at the TOA and of about 0.55 W/m² (53%) at SFC.

Results from the opaque cirrus cloud (Fig. 4b, left and right panels) exhibit a similar behavior to the thin cirrus cloud, with signal smoothing being outweighing lidar technique (blue arrow). The order of magnitude is similar to the thin cirrus cloud, with a difference at TOA between techniques of 0.8 W/m² (3%) and 0.38 W/m² (3%) at SFC. In contrast, the difference in data processing is of 11.8 W/m² (39%) at TOA and 7.7 W/m² (64%) at SFC. The results are evidence of the critical need to study cirrus clouds using

high-resolution profiles of the optical properties to provide an accurate estimation of the cloud direct radiative effect.

4. Conclusions and future perspectives

We applied the adapted Fu-Liou-Gu (FLG) radiative transfer model to quantitatively evaluate how much the lidar technique and/or data processing influence the net direct radiative effect exerted by two different upper atmospheric aerosol layers (dust and biomass burning) and a thin and opaque cirrus cloud layer, both at top-of-the-atmosphere (TOA) and surface (SFC). The evaluation has been made using the aerosol/cloud extinction atmospheric profile as inputs into FLG radiative transfer model retrieved using the Raman/elastic technique and estimated by lidar elastic measurements only (iterative method for aerosol layers and thin cirrus cloud; MPLNET Level 1.5 cloud algorithm for opaque cirrus cloud). Because the Raman measurement retrieval is unstable due to the derivative of the signal at the numerator (see Eq. 2), a smoothing of the range-corrected signal is necessary to reduce the associated random uncertainty. The same processing treatment has been applied also to the elastic measurement signals.

The results show that the difference in direct radiative effect between the techniques and data processing/smoothing applied is mostly unvaried at TOA and SFC. For the dust and biomass burning episodes, the data processing/smoothing does not play a major role, but instead the lidar measurement technique is more important with respect to the final result. This can be explained by the large variability of the lidar ratio (i.e., the unknown extinction-to-backscatter ratio used to constrain the single-solution lidar equation) compared to the assumed value. The opposite is true for cirrus clouds, where the applied

data processing/smoothing play a fundamental role in determining sensitivities in the final results. This is due to the smoothing effect on the observed sharp structures that strongly alters the vertical structure and the extinction of the cloud.

Summarizing, we found that for the aerosol cases, the main difference both at TOA and SFC is driven by the different lidar technique and not the data processing with a difference on dust direct radiative effect of 0.7 W/m^2 (5%) at SFC and 0.85 W/m^2 (6%) at TOA. Similarly, for biomass burning we found a discrepancy 0.05 W/m^2 (5%) at SFC and 0.007 W/m^2 (5%) at TOA. On the contrary, for the cirrus clouds, the data smoothing is producing larger differences with respect to the lidar technique. On the contrary, using a different data processing/smoothing implies a larger difference in cirrus cloud direct radiative effect. A discrepancy of 0.55 W/m^2 (53%) is found at SFC while about 2.7 W/m^2 (47%) at TOA for the thin cirrus cloud. Similarly, for the opaque cirrus the discrepancies produced by data processing/smoothing is larger with respect to the different lidar technique. At SFC we have a difference of 7.7 W/m^2 (64%) and 11.8 W/m^2 at TOA (39%). A possible explanation of this different behavior is that the FLG radiative transfer model calculations are strongly dependent on the optical depth of the examined atmospheric layer. At coarse resolution (cloud) the smoothing is producing changes in the extinction profile that translates into creation/suppression of ice crystals that have a strong influence on direct radiative effect. At finer resolution, as in the case of aerosol case studies, the smoothing is just producing fluctuations that do not influence the total radiative effect. In this case, the lidar technique is making a big difference, as an assumed wrong value for lidar ratio (S) that has a much larger variability with respect to the

clouds, will amplify or suppress the aerosol peak that will translate into a higher/lower radiative effect.

With this study, we wish to draw attention in speculating how much derived aerosol and cloud radiative effect behaviors are dependent on lidar measurement and retrieval techniques as well as on the data processing constraints/assumptions. This dependence looks relevant for existing and future space missions involving lidar instrument, as well as for the GAW Atmospheric Lidar Observation Network (GALION; Hoff et al., 2008) project, which has as main objective to federate all the existing ground-based lidar networks to provide atmospheric measurement profiles of the aerosol and cloud optical and microphysical properties with sufficient coverage, accuracy and resolution. For future work, it is imperative on the community to continue understanding and refining what are the limits of the each lidar technique along with the related retrieval algorithms adopted in each ground-based network. FLG or any other well-established radiative transfer model then can be used as diagnostic tool to assure data quality through continued intercomparisons with real observation both at ground (using flux measurements), in situ (aircraft measurements) and at TOA (using satellite-based measurements).

References

- Ackermann J., 1998: The Extinction-to-Backscatter Ratio of Tropospheric Aerosol: A Numerical Study. *J. Atmos. Oceanic Technol.*, **15**, 1043–1050.
- Ansmann, A., M. Riebesell, and C. Weitkamp, 1990: Measurement of atmospheric aerosol extinction profiles with a Raman lidar. *Opt. Lett.*, **15**, 746–748

406 Ansmann, A., Wandinger, U., Riebesell, M., Weitkamp, C., Michaelis, W., 1992,”
 407 Independent measurement of extinction and backscatter profiles in cirrus clouds
 408 by using a combined raman elastic-backscatter lidar”, *Applied Optics*, 31 (33), pp.
 409 7113-7131

410 Ansmann, A. and Müller, D., 2005 “Lidar and atmospheric aerosol particles”, in: *LIDAR –*
 411 *Range-resolved optical remote sensing of the atmosphere*, edited by: Weitkamp,
 412 C., Springer, New York, USA, 105–141

413 Antuña-Marrero, J.C., E. Landulfo, R. Estevan, B. Barja, A. Robock, E. Wolfram, P.
 414 Ristori, B. Clemesha, F. Zaratti, R. Forno, E. Armandillo, Á.E. Bastidas, Á.M. de
 415 Frutos Baraja, D.N. Whiteman, E. Quel, H.M. Barbosa, F. Lopes, E. Montilla-
 416 Rosero, and J.L. Guerrero-Rascado, 0: LALINET: The first Latin American-born
 417 regional atmospheric observational network. *Bull. Amer. Meteor. Soc.*, **0**, doi:
 418 10.1175/BAMS-D-15-00228.1.

419 Asmi, A., Collaud Coen, M., Ogren, J. A., Andrews, E., Sheridan, P., Jefferson, A., ... &
 420 Kivekäs, N. (2013). Aerosol decadal trends–Part 2: In-situ aerosol particle
 421 number concentrations at GAW and ACTRIS stations. *Atmospheric Chemistry*
 422 *and Physics*, 13(2), 895-916.

423 Bösenberg, J and R Hoff ,2008 GAW Aerosol Lidar Observation Network (GALION),
 424 WMO GAW Report (WMO, Geneva, Switzerland)

425 Campbell, J. R., D. L. Hlavka, E. J. Welton, C. J. Flynn, D. D. Turner, J. D. Spinhirne, V.
 426 S. Scott III, and I. H. Hwang, 2002. "Full-time, eye-safe cloud and aerosol lidar
 427 observation at atmospheric radiation measurement program sites: Instruments and
 428 data processing." *Journal of Atmospheric and Oceanic Technology* 19, no. 4: 431-

429 Campbell, J.R., S. Lolli, J.R. Lewis, Y. Gu, and E.J. Welton, 2016, "Daytime Cirrus
 430 Cloud Top-of-the-Atmosphere Radiative Forcing Properties at a Midlatitude Site
 431 and Their Global Consequences", *Journal of Applied Meteorology and*
 432 *Climatology*, 55, 8, 1667-1679

433 Comstock, J. M., S. A. McFarlane, R. d'Entremont, D. DeSlover, D.D. Turner, G.G.
 434 Mace, S.Y. Matrosov, M.D. Shupe, P. Minnis, D. Mitchell, K. Sassen, and Z.
 435 Wang, 2007:An Intercomparison of Microphysical Retrieval Algorithms for
 436 Upper-Tropospheric Ice Clouds. *Bull. Amer. Meteor. Soc.*, **88**, 191–
 437 204, <https://doi.org/10.1175/BAMS-88-2-191>

438 d'Almeida, G. A., Koepke, P., and Shettle, E. P.: Atmospheric aerosols – global
 439 climatology and radiative characteristics, A. Deepak Publishing, Hampton,
 440 Virginia, 561 pp., 1991.

441 Di Girolamo, P., P. F. Ambrico, A. Amodeo, A. Boselli, G. Pappalardo, and N. Spinelli,
 442 Aerosol observations by lidar in the nocturnal boundary layer, *Appl. Opt.*, 38
 443 (21), 4585–4595, 1999.

444 Illingworth, A. J., Hogan, R. J., O'connor, E. J., Bouniol, D., Delanoë, J., Pelon, J., ... &
 445 Donovan, D. P. (2007). Cloudnet: Continuous evaluation of cloud profiles in
 446 seven operational models using ground-based observations. *Bulletin of the*
 447 *American Meteorological Society*, 88(6), 883-898.

448 Diner, D.J., Beckert, J.C., Reilly, T.H., Bruegge, C.J., Conel, J.E., Kahn, R.A.,
 449 Martonchik, J.V., Ackerman, T.P., Davies, R., Gerstl, S.A.W., Gordon, H.R.,
 450 Muller, J.-P., Myneni, R.B., Sellers, P.J., Pinty, B., Verstraete, M.M. Multi-angle
 451 imaging spectroradiometer (MISR) instrument description and experiment

452 overview (1998) IEEE Transactions on Geoscience and Remote Sensing, 36 (4),
 453 pp. 1072-1087

454 Di Girolamo, L., T. C. Bond, D. Bramer, D. J. Diner, F. Fettinger, R. A. Kahn, J. V.
 455 Martonchik, M. V. Ramana, V. Ramanathan, and P. J. Rasch. "Analysis of Multi-
 456 angle Imaging SpectroRadiometer (MISR) aerosol optical depths over greater
 457 India during winter 2001–2004." *Geophysical Research Letters* 31, no. 23 (2004).

458 Dubovik, O., Smirnov, A., Holben, B. N., King, M. D., Kaufman, Y. J., Eck, T. F., &
 459 Slutsker, I. (2000). Accuracy assessments of aerosol optical properties retrieved
 460 from Aerosol Robotic Network (AERONET) Sun and sky radiance
 461 measurements. *Journal of Geophysical Research: Atmospheres*, 105(D8), 9791-
 462 9806.

463 Eck, T. F., Holben, B. N., Reid, J. S., Arola, A., Ferrare, R. A., Hostetler, C. A., ... &
 464 Lyapustin, A. (2014). Observations of rapid aerosol optical depth enhancements
 465 in the vicinity of polluted cumulus clouds. *Atmospheric Chemistry and*
 466 *Physics*, 14(21), 11633.

467 Ferrare, R., Feingold, G., Ghan, S., Ogren, J., Schmid, B., Schwartz, S.E. and Sheridan,
 468 P., 2006. Preface to special section: Atmospheric Radiation Measurement
 469 Program May 2003 Intensive Operations Period examining aerosol properties and
 470 radiative influences. *Journal of Geophysical Research: Atmospheres*, 111(D5).

471 Fu Q, Liou KN, 1992: On the correlated k-distribution method for radiative transfer in
 472 nonhomogeneous atmospheres. *J. Atmos. Sci.* 49:2139-2156.

473 Fu Q, Liou KN, 1993: Parametrization of the radiative properties of cirrus clouds. *J.*
 474 *Atmos. Sci.* 50:2008-2025.

475 Goldsmith, J. E. M., F. H. Blair, S. E. Bisson, and D. D. Turner, 1998: Turn-Key Raman
 476 lidar for profiling atmospheric water vapor, clouds, and aerosols. *Appl. Opt.*, **37**,
 477 4979–4990.

478 Grund, C. J. and E. W. Eloranta, 1991 "University of Wisconsin High Spectral Resolution
 479 Lidar," *Optical Engineering*, **30**, 6--12, 1991.

480 Gu Y, Farrara J, Liou KN, Mechoso CR, 2003: Parametrization of cloud-
 481 radiative processes in the UCLA general circulation model. *J. Climate* 16:3357-
 482 3370.

483 Gu Y, Liou KN, Ou SC, Fovell R, 2011: Cirrus cloud simulations using WRF
 484 with improved radiation parametrization and increased vertical resolution. *J.*
 485 *Geophys. Res.* 116:D06119.

486 Hess, M., Koepke, P., and Schult, I.: Optical properties of aerosols and clouds: The
 487 software package OPAC, *B. Am. Meteorol. Soc.*, 79, 831–844, 1998.

488 Heymsfield, A., D. Winker, M. Avery, M. Vaughan, G. Diskin, M. Deng, V. Mitev, and
 489 R. Matthey, 2014: Relationships between ice water content and volume extinction
 490 coefficient from in situ observations for temperatures from 0° to –86°C:
 491 Implications for spaceborne lidar retrievals. *J. Appl. Meteor. Climatol.*, 53, 479–
 492 505

493 Hoff, R. M., Bösenberg, J., & Pappalardo, G. (2008, June). The GAW Aerosol Lidar
 494 Observation Network (GALION). In Reviewed and Revised Papers Presented at
 495 the 24th International Laser Radar Conference (pp. 23-27).

496 Iarlori, M., Madonna, F., Rizi, V., Trickl, T., and Amodeo, A., 2015: Effective resolution
497 concepts for lidar observations, *Atmos. Meas. Tech.*, 8, 5157-5176,
498 doi:10.5194/amt-8-5157-2015.

499 Illingworth, A.J., Barker, H.W., Beljaars, A., Ceccaldi, M., Chepfer, H., Clerbaux, N.,
500 Cole, J., Delanoë, J., Domenech, C., Donovan, D.P., Fukuda, S., Hirakata, M.,
501 Hogan, R.J., Huenerbein, A., Kollias, P., Kubota, T., Nakajima, T., Nakajima,
502 T.Y., Nishizawa, T., Ohno, Y., Okamoto, H., Oki, R., Sato, K., Satoh, M.,
503 Shephard, M.W., Velázquez-Blázquez, A., Wandinger, U., Wehr, T., Van
504 Zadelhoff, G.-J. The earthcare satellite: The next step forward in global
505 measurements of clouds, aerosols, precipitation, and radiation (2015) *Bulletin of*
506 *the American Meteorological Society*, 96 (8), pp. 1311-1332

507 IPCC, 2012: Managing the Risks of Extreme Events and Disasters to Advance Climate
508 Change Adaptation. A Special Report of Working Groups I and II of the
509 Intergovernmental Panel on Climate Change [Field, C.B., V. Barros, T.F. Stocker,
510 D. Qin, D.J. Dokken, K.L. Ebi, M.D. Mastrandrea, K.J. Mach, G.-K. Plattner,
511 S.K. Allen, M. Tignor, and P.M. Midgley (eds.)]. Cambridge University Press,
512 Cambridge, UK, and New York, NY, USA, 582 pp.

513 IPCC, 2014: Climate Change 2014: Impacts, Adaptation, and Vulnerability. Part A:
514 Global and Sectoral Aspects. Contribution of Working Group II to the Fifth
515 Assessment Report of the Intergovernmental Panel on Climate Change [Field,
516 C.B., V.R. Barros, D.J. Dokken, K.J. Mach, M.D. Mastrandrea, T.E. Bilir, M.
517 Chatterjee, K.L. Ebi, Y.O. Estrada, R.C. Genova, B. Girma, E.S. Kissel, A.N.

518 Levy, S. MacCracken, P.R. Mastrandrea, and L.L. White (eds.)]. *Cambridge*
 519 *University Press, Cambridge, United Kingdom and New York, NY, USA*, 1132 pp.

520 Kahn, R. A., David L. Nelson, Michael J. Garay, Robert C. Levy, Michael A. Bull, David
 521 J. Diner, John V. Martonchik, Susan R. Paradise, Earl G. Hansen, and Lorraine A.
 522 Remer. "MISR aerosol product attributes and statistical comparisons with
 523 MODIS." *IEEE Transactions on Geoscience and Remote Sensing* 47, no. 12
 524 (2009): 4095-4114

525 Khor W. Y, Matjafri M. Z., Lim H.; Hee W. S ; Lolli S., 2015: One-year monitoring of
 526 the atmosphere over Penang Island using a ground-based lidar *Proc. SPIE 9645*,
 527 *Lidar Technologies, Techniques, and Measurements for Atmospheric Remote*
 528 *Sensing XI*, 96450M (October 20, 2015); doi:10.1117/12.2195440.

529 King, Michael D., W. Paul Menzel, Yoram J. Kaufman, Didier Tanré, Bo-Cai Gao,
 530 Steven Platnick, Steven A. Ackerman, Lorraine A. Remer, Robert Pincus, and
 531 Paul A. Hubanks, 2003 "Cloud and aerosol properties, precipitable water, and
 532 profiles of temperature and water vapor from MODIS." *IEEE Transactions on*
 533 *Geoscience and Remote Sensing* 41, no. 2: 442-458.

534 J. Klett, 1985, "Lidar inversion with variable backscatter/extinction ratios," *Appl. Opt.*
 535 24, 1638-1643.

536 Lewis, J. R., J. R. Campbell, E. J. Welton, S. A. Stewart, and P. C. Haftings, 2016:
 537 Overview of MPLNET, version 3, cloud detection. *J. Atmos. Oceanic Technol.*,
 538 33, 2113–2134, doi: 10.1175/JTECH-D-15-0190.1

539 Lolli S. et al, 2013, "Evaluating light rain drop size estimates from multiwavelength
 540 micropulse lidar network profiling," *J. Atmos. Oceanic Technol.*, **30**, 2798–2807.

541 Lolli S. ; E. J. Welton ; A. Benedetti ; L. Jones ; M. Suttie ; S-H. Wang. 2014.” MPLNET
 542 lidar data assimilation in the ECMWF MACC-II Aerosol system: evaluation of
 543 model performances at NCU lidar station.” *Proc. SPIE 9246, Lidar Technologies,*
 544 *Techniques, and Measurements for Atmospheric Remote Sensing X*, 92460I
 545 (October 20, 2014); doi:10.1117/12.2068201
 546 S. Lolli; P. Di Girolamo. 2015.” Principal component analysis approach to evaluate
 547 instrument performances in developing a cost-effective reliable instrument
 548 network for atmospheric measurements.” *Journal of Atmospheric and Oceanic*
 549 *Technology*, Vol. 32 (9), 1642-1649.
 550 Lolli, S., J.R. Campbell, J.R. Lewis, Y. Gu, J.W. Marquis, B.N. Chew, S. Liew, S.V.
 551 Salinas, and E.J. Welton, 2017a: Daytime Top-of-the-Atmosphere Cirrus Cloud
 552 Radiative Forcing Properties at Singapore. *J. Appl. Meteor. Climatol.*, **56**, 1249–
 553 1257, doi: 10.1175/JAMC-D-16-0262.1.
 554 Lolli, S., Campbell, J. R., Lewis, J. R., Gu, Y., and Welton, E. J. 2017b: Technical note:
 555 Fu–Liou–Gu and Corti–Peter model performance evaluation for radiative
 556 retrievals from cirrus clouds, *Atmos. Chem. Phys.*, 17, 7025-7034,
 557 <https://doi.org/10.5194/acp-17-7025-2017>.
 558 Madonna, F., Amodeo, A., Boselli, A., Cornacchia, C., Cuomo, V., D'Amico, G., Giunta,
 559 A., Mona, L., and Pappalardo, G.: CIAO: the CNR-IMAA advanced observatory
 560 for atmospheric research, *Atmos. Meas. Tech.*, 4, 1191-1208, doi:10.5194/amt-4-
 561 1191-2011, 2011.

562 Madonna, F., A. Amodeo, G. D'Amico, and G. Pappalardo (2013), A study on the use of
563 radar and lidar for characterizing ultragiant aerosol, *Journal of Geophys. Res.*,
564 DOI: 10.1002/jgrd.50789.

565 Madonna F., A. Amodeo, G. D'Amico, L. Mona, and G. Pappalardo (2010), Observation
566 of non-spherical ultragiant aerosol using a microwave radar, *Geophys. Res. Lett.*,
567 37, L21814, doi:10.1029/2010GL044999.

568 McComiskey, A. and R.A. Ferrare, 2016: Aerosol Physical and Optical Properties and
569 Processes in the ARM Program. *Meteorological Monographs*, **57**, 21.1–21.17,

570 McGill, M.J., Yorks, J.E., Scott, V.S., Kupchock, A.W., Selmer, P.A. The Cloud-Aerosol
571 Transport System (CATS): A technology demonstration on the International
572 Space Station (2015) *Proceedings of SPIE - The International Society for Optical*
573 *Engineering*, 9612, art. no. 96120A

574 Mona, L., Amodeo, A., Pandolfi, M., & Pappalardo, G., 2006. Saharan dust intrusions in
575 the Mediterranean area: Three years of Raman lidar measurements. *Journal of*
576 *Geophysical Research: Atmospheres*, *111*(D16).

577 Mona, L., Amodeo, A., D'Amico, G., Giunta, A., Madonna, F., & Pappalardo, G. 2012.
578 Multi-wavelength Raman lidar observations of the Eyjafjallajökull volcanic cloud
579 over Potenza, southern Italy. *Atmospheric Chemistry and Physics*, *12*(4), 2229-
580 2244.

581 Pappalardo, G., Amodeo, A., Mona, L., Pandolfi, M., Pergola, N., & Cuomo, V. (2004).
582 Raman lidar observations of aerosol emitted during the 2002 Etna
583 eruption. *Geophysical Research Letters*, *31*(5).

584 Pappalardo, G., Amodeo, A., Apituley, A., Comeron, A., Freudenthaler, V., Linné, H.,
 585 Ansmann, A., Bösenberg, J., D'Amico, G., Mattis, I., Mona, L., Wandinger, U.,
 586 Amiridis, V., Alados-Arboledas, L., Nicolae, D., and Wiegner, M., 2014.
 587 EARLINET: towards an advanced sustainable European aerosol lidar network,
 588 *Atmos. Meas. Tech.*, 7, 2389-2409, doi:10.5194/amt-7-2389-2014,

589 Pappalardo G., A. Amodeo, M. Pandolfi, U. Wandinger, A. Ansmann, J. Bosenberg, V.
 590 Matthias, V. Amiridis, F. De Tomasi, M. Frioud, M. Iarlori, L. Komguem, A.
 591 Papayannis, F. Rocadenbosch, and X. Wang, 2004 “Aerosol lidar intercomparison
 592 in the framework of the EARLINET, project. 3. Raman lidar algorithm for aerosol
 593 extinction, backscatter and lidar ratio”, *Appl. Opt.*, 43(28), 5370–5385.

594 Pérez-Ramírez, D., Whiteman, D.N., Smirnov, A., Lyamani, H., Holben, B.N., Pinker,
 595 R., Andrade, M. and Alados-Arboledas, L., 2014. Evaluation of AERONET
 596 precipitable water vapor versus microwave radiometry, GPS, and radiosondes at
 597 ARM sites. *Journal of Geophysical Research: Atmospheres*, 119(15), pp.9596-
 598 9613.

599 Press, W.H., B. P. Flannery, S. A. Teukolsky, and W. T. Vetterling, 1992 “Numerical
 600 Recipes in FORTRAN: The Art of Scientific Computing”, 2nd ed., Cambridge,
 601 U. Press, Cambridge, pp. 127–128 and 644–647.

602 Remer, L.A., Kaufman, Y.J., Tanré, D., Mattoo, S., Chu, D.A., Martins, J.V., Li, R.-R.,
 603 Ichoku, C., Levy, R.C., Kleidman, R.G., Eck, T.F., Vermote, E., Holben, B.N.
 604 The MODIS aerosol algorithm, products, and validation 2005, *Journal of*
 605 *Atmospheric Sciences*, 62 (4), pp. 947-973

606 Strahler, A. H., C. B. Schaaf, J.-P. Muller, W. Warmer, M. J. Barnsley, R. d'Entremont,
607 B. Hu, P. Lewis, X. Li, and E. V. Ruiz de Lope, 1999: MODIS BRDF/albedo
608 product: Algorithm theoretical basis document. *NASA EOS-MODIS Doc. ATBD-*
609 *MOD-09*, version 5.0

610 Sugimoto, N., Matsui, I., Shimizu, A., Nishizawa, T., Hara, Y., Uno, I. Lidar network
611 observation of tropospheric aerosols (2010) *Proceedings of SPIE - The*
612 *International Society for Optical Engineering*, 7860, art. no. 78600J

613 Smirnov, A., Holben, B. N., Eck, T. F., Slutsker, I., Chatenet, B., & Pinker, R. T. (2002).
614 Diurnal variability of aerosol optical depth observed at AERONET (Aerosol
615 Robotic Network) sites. *Geophysical Research Letters*, 29(23).

616 Tanré, D., Y. J. Kaufman, M. Herman, and S. Mattoo. "Remote sensing of aerosol
617 properties over oceans using the MODIS/EOS spectral radiances." *Journal of*
618 *Geophysical Research: Atmospheres* 102, no. D14 (1997): 16971-16988.

619 Tanré, D., F. M. Bréon, J. L. Deuzé, O. Dubovik, F. Ducos, P. François, P. Goloub, M.
620 Herman, A. Lifermann, and F. Waquet. "Remote sensing of aerosols by using
621 polarized, directional and spectral measurements within the A-Train: the
622 PARASOL mission." *Atmospheric Measurement Techniques* 4, no. 7 (2011):
623 1383-1395.

624 Tegen, I. and Lacis, A. A.: Modeling of particle size distribution and its influence on the
625 radiative properties of mineral dust aerosol, *J. Geophys. Res.*, 101, 19237–19244,
626 1996.

627 Veselovskii, I., Whiteman, D.N., Korenskiy, M., Suvorina, A., Pérez-Ramírez, D., (2015)
628 Use of rotational Raman measurements in multiwavelength aerosol lidar for

629 evaluation of particle backscattering and extinction. *Atmospheric Measurement*
 630 *Techniques* 8, 4111-4122.

631 Wandinger, U., Ansmann, A., Reichardt, J., Dethler, T. Determination of stratospheric
 632 aerosol microphysical properties from independent extinction and backscattering
 633 measurements with a Raman lidar (1995) *Applied Optics*, 34 (36), pp. 8315-8329.

634 Wandinger, U., Freudenthaler, V., Baars, H., Amodeo, A., Engelmann, R., Mattis, I.,
 635 Gross, S., Pappalardo, G., Giunta, A., D'Amico, G., Chaikovsky, A., Osipenko,
 636 F., Slesar, A., Nicolae, D., Belegante, L., Talianu, C., Serikov, I., Linn, H.,
 637 Jansen, F., Apituley, A., Wilson, K. M., de Graaf, M., Trickl, T., Giehl, H., Adam,
 638 M., Comerón, A., Muñoz-Porcar, C., Rocadenbosch, F., Sicard, M., Tomás, S.,
 639 Lange, D., Kumar, D., Pujadas, M., Molero, F., Fernández, A. J., Alados-
 640 Arboledas, L., Bravo-Aranda, J. A., Navas-Guzmán, F., Guerrero-Rascado, J. L.,
 641 Granados-Munoz, M. J., Preiler, J., Wagner, F., Gausa, M., Grigorov, I.,
 642 Stoyanov, D., Iarlori, M., Rizi, V., Spinelli, N., Boselli, A., Wang, X., Lo Feudo,
 643 T., Perrone, M. R., De Tomasi, F., and Burlizzi, P., 2016: EARLINET instrument
 644 intercomparison campaigns: overview on strategy and results, *Atmos. Meas.*
 645 *Tech.*, 9, 1001-1023, doi:10.5194/amt-9-1001-2016

646 Whiteman, D. N., Melfi, S. H., & Ferrare, R. A. (1992). Raman lidar system for the
 647 measurement of water vapor and aerosols in the Earth's atmosphere. *Applied*
 648 *Optics*, 31(16), 3068-3082.

649 Whiteman, D.N. Examination of the traditional Raman lidar technique. II. Evaluating the
 650 ratios for water vapor and aerosols (2003) *Applied Optics*, 42 (15), pp. 2593-2608

651 Whiteman, D.N., Pérez-Ramírez, D., Veselovskii, I., Colarco, P., Buchard, V. (2017)
652 Simulations of spaceborne multiwavelength lidar measurements and retrievals of
653 aerosol microphysics. *Journal of Quantitative Spectroscopy and Radiative*
654 *Transfer*, submitted.

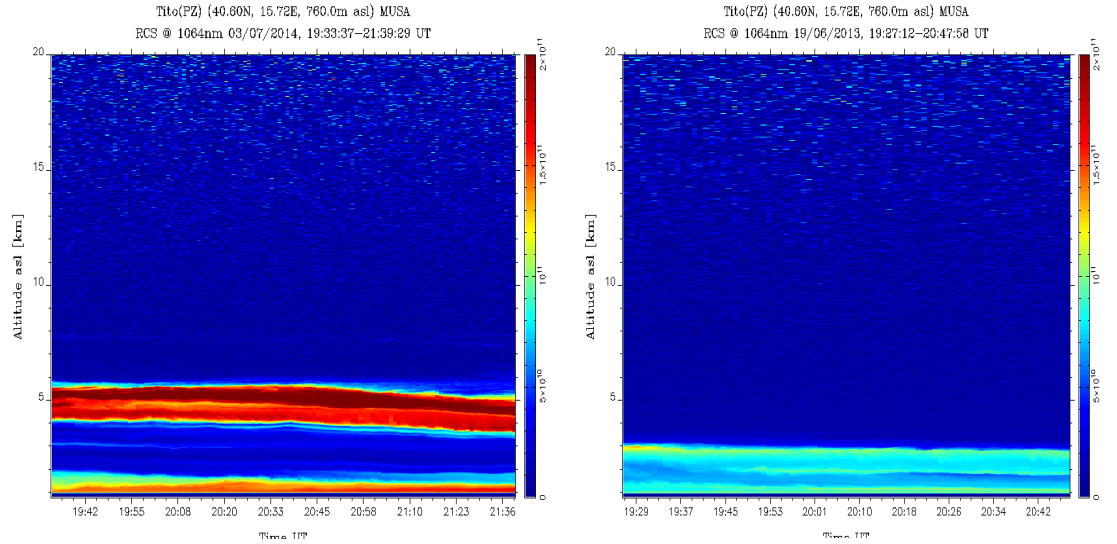
655 Winker, D. M., W. H. Hunt, and M. J. McGill (2007), Initial performance assessment of
656 CALIOP, *Geophys. Res. Lett.*, 34, L19803, doi:10.1029/2007GL030135.

657 Welton, E. J., Voss, K. J., Quinn, P. K., Flatau, P. J., Markowicz, K., Campbell, J. R.,
658 Johnson, J. E. 2002. Measurements of aerosol vertical profiles and optical
659 properties during INDOEX 1999 using micropulse lidars. *Journal of Geophysical*
660 *Research: Atmospheres*, 107(D19).

661

Figures

a)



b)

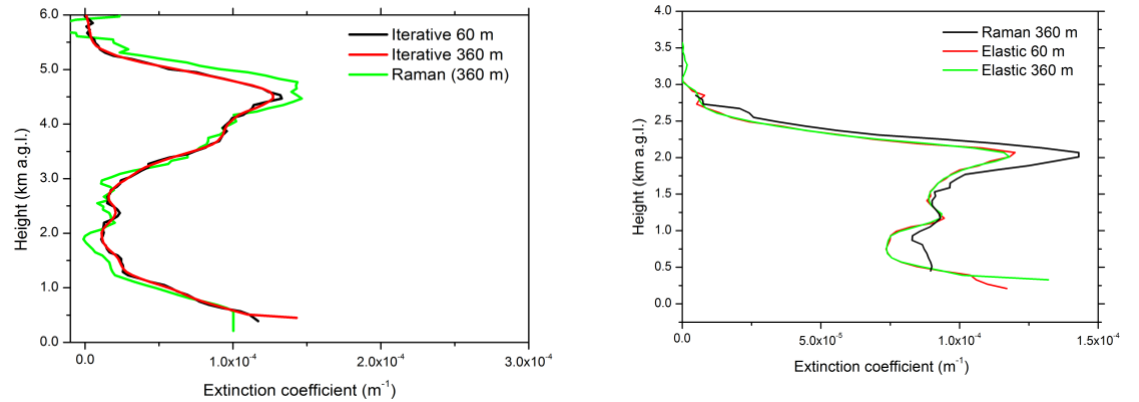


Figure 1 a): composite plot of

the range corrected signal at 1064nm showing a well-defined dust layer at about 5 km a.s.l. (left panel) and for a biomass burning aerosol layer at about 2 km (right panel). b): aerosol lidar extinction profiles at 355nm retrieved with the Raman and the elastic lidar techniques with different spatial resolutions (60m and 360m) for dust outbreak on 3 July 2014 (left panel) and for biomass burning on 19 June 2013 (right panel). The iterative method used a fixed lidar ratio value of $S=45\text{sr}$, determined by climatological measurements (Mona et al., 2006) for the dust aerosol layer. For the biomass burning we used the averaged value of $S=63\text{sr}$ obtained from MUSA Raman lidar.

689

a)

691

692

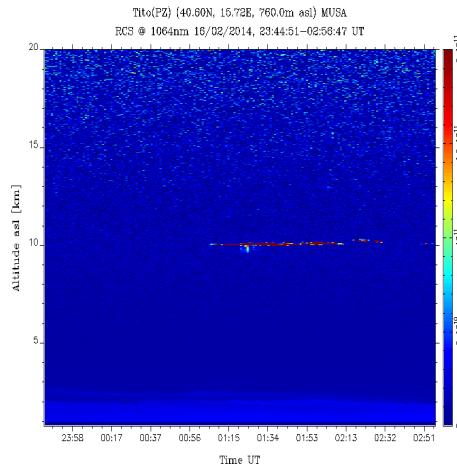
693

694

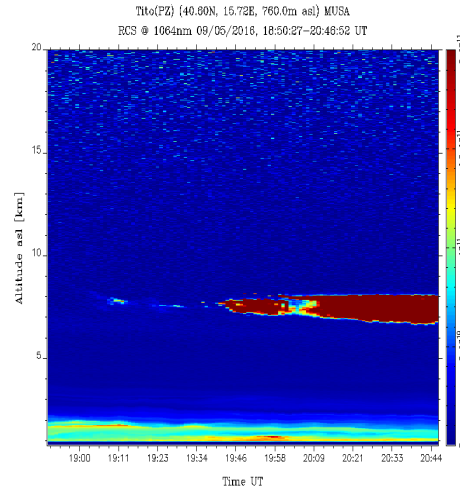
695

696

697



690



b)

698

699

700

701

702

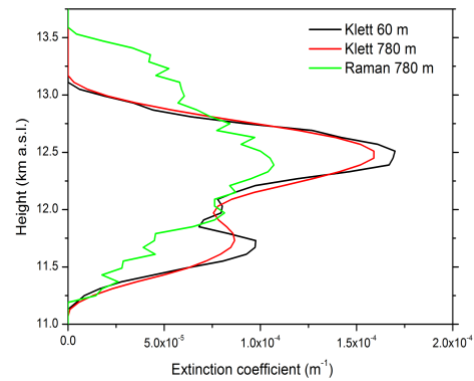
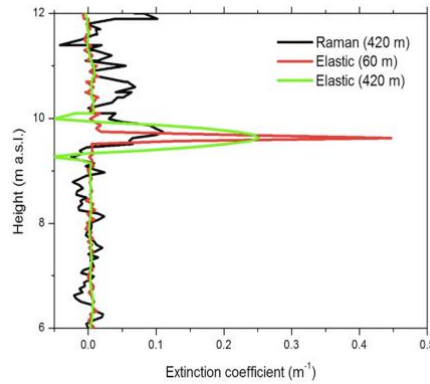
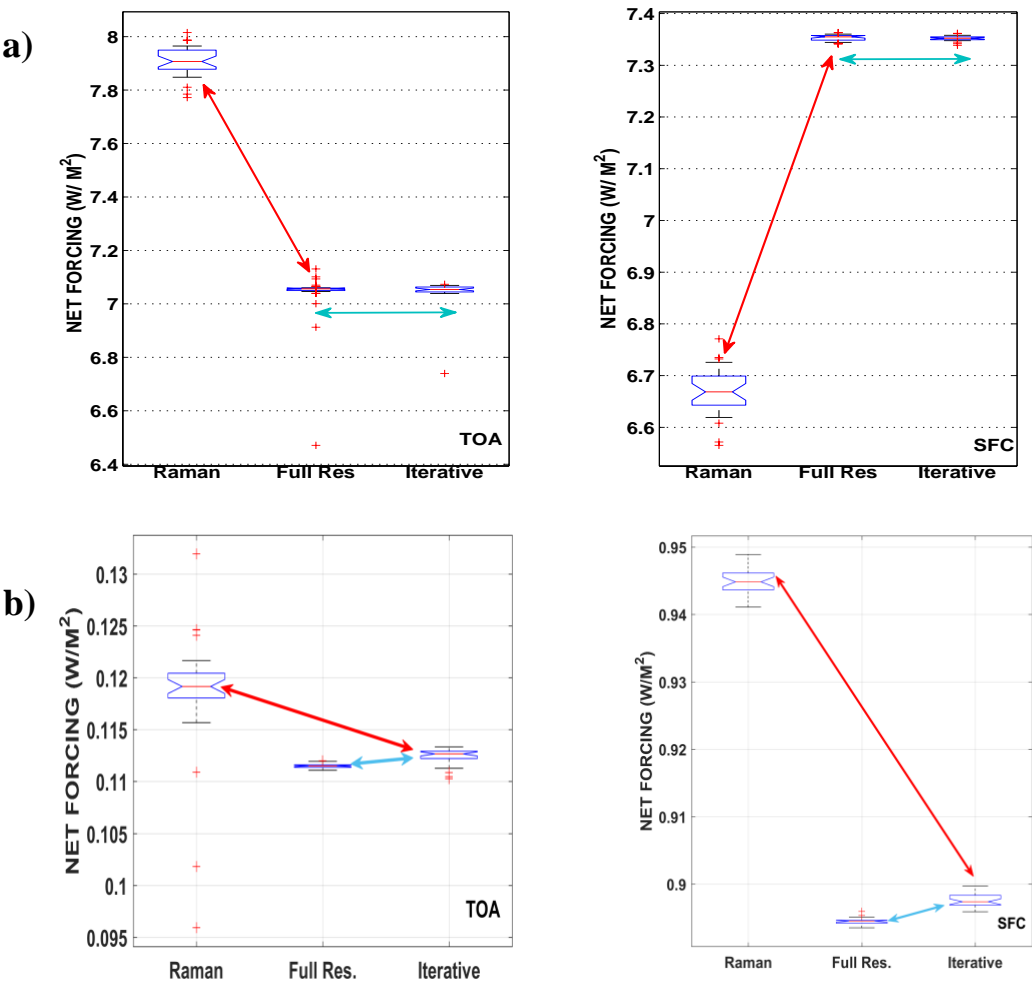
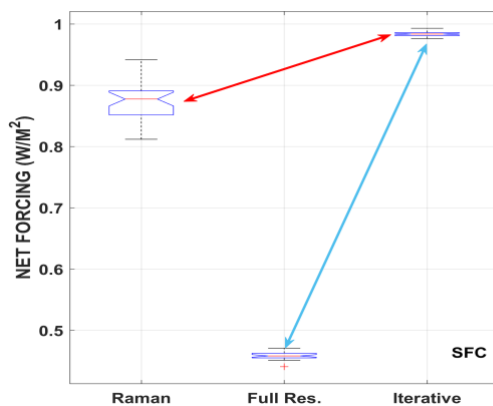
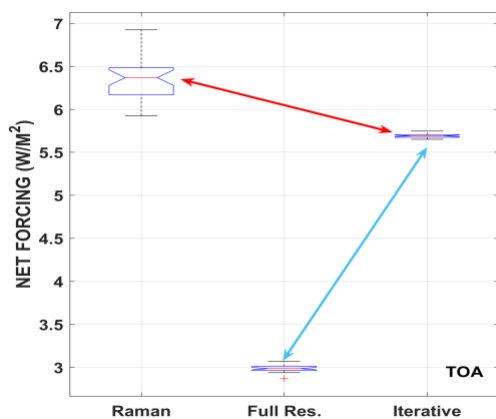


Figure 2: a) composite plot of the range corrected signal at 1064nm showing a thin cirrus cloud at about 10km (right panel) and an opaque cirrus cloud at about 12.5 km. b) left panel: lidar extinction profiles at 355nm from Raman and elastic channel respectively a cirrus cloud on 17 February 2014. The iterative method at the two different resolutions (60m and 420m) used a fixed S value (25sr), determined by climatological measurement. Figure 2a, b) right panels: same as Figure 2a, b) left panels but for a cirrus cloud detected on 09 May 2016. The Raman is retrieved over a 780m spatial window while the elastic channel is retrieved using MPLNET algorithm (Lewis et al., 2016) with $S=25sr$ at 60m and 780m respectively.



713 Figure 3. The direct radiative effect, for the dust aerosol case study (Figure 3a) on 03 July 2014 and
714 biomass burning case on 19 June 2013(Figure 3b) represented as a distribution of values obtained with the
715 MonteCarlo simulations by the boxplots, is calculated at TOA (left panel) and SFC (right panel)
716 respectively. As it is clearly visible, the larger discrepancy in forcing is related mostly to the lidar
717 measurements technique (red arrows), not on the data processing constraints/assumptions (blue arrows).
718

a)



b)

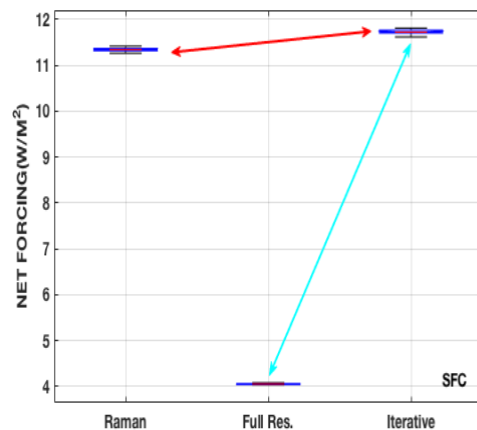
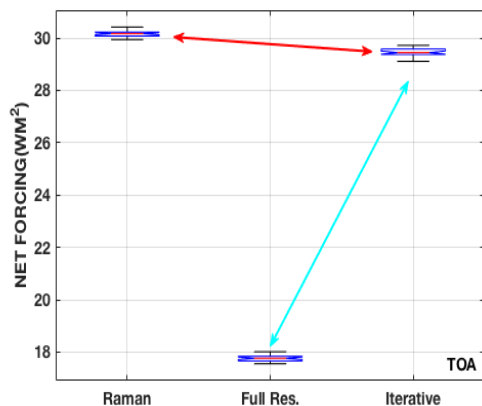


Figure 4 Same as Figure 3 but for two cirrus cloud cases (Fig. 4a, 17 Feb 2014, Fig 4b, 09 May 2016). The net radiative effect is calculated at TOA (left panel) and SFC (right panel) respectively. As it is clearly visible, in both cases the larger discrepancy in radiative effect is related mostly to the data processing (blue arrows), not on lidar technique (red arrows).